Influence investigation of a void region on modeling light propagation in a heterogeneous medium

6 authors, including:

Xueli Chen
Xidian University
48 PUBLICATIONS **308** CITATIONS

SEE PROFILE

Xiaochao Qu
Xidian University
47 PUBLICATIONS **593** CITATIONS

SEE PROFILE

Jie Tian
Chinese Academy of Sciences
661 PUBLICATIONS **7,099** CITATIONS

SEE PROFILE

Jimin Liang
Xidian University
164 PUBLICATIONS **1,520** CITATIONS

SEE PROFILE

Influence investigation of a void region on modeling light propagation in a heterogeneous medium

Defu Yang,[1] Xueli Chen,[1] Shenghan Ren,[1] Xiaochao Qu,[1] Jie Tian,[1,2] and Jimin Liang[1,*]

[1]School of Life Sciences and Technology, Xidian University, Xi'an, Shaanxi 710126, China

[2]Institute of Automation, Chinese Academy of Sciences, Beijing 100190, China

*Corresponding author: jimleung@mail.xidian.edu.cn

A void region exists in some biological tissues, and previous studies have shown that inaccurate images would be obtained if it were not processed. A hybrid radiosity–diffusion method (HRDM) that couples the radiosity theory and the diffusion equation has been proposed to deal with the void problem and has been well demonstrated in two-dimensional and three-dimensional (3D) simple models. However, the extent of the impact of the void region on the accuracy of modeling light propagation has not been investigated. In this paper, we first implemented and verified the HRDM in 3D models, including both the regular geometries and a digital mouse model, and then investigated the influences of the void region on modeling light propagation in a heterogeneous medium. Our investigation results show that the influence of the region can be neglected when the size of the void is less than a certain range, and other cases must be taken into account.   © 2013 Optical Society of America

OCIS codes: 170.3660, 170.3880.

1. Introduction

Modeling light propagation in biological tissues provides a basis for solving the inverse problem of three-dimensional (3D) optical imaging, a rapidly growing and promising imaging modality that has obtained wide application and become a valuable tool for the field of biomedical imaging [1–5]. It is well acknowledged that light propagation in biological tissues can be accurately expressed by the radiative transfer equation (RTE) [6,7]. However, RTE is a complicated integral–differential equation, which is hard to solve in the complicated 3D irregular medium and needs expensive computational time and memory [2,7]. To address this problem, several approximation models of the RTE were proposed, which have been effectively and commonly used in optical tomography, such as the diffusion equation (DE) [8], the discrete ordinates equation (S_N) [9,10], the

spherical harmonics equation (P_N) [11], the phase approximation (PA) [12], and the simplified spherical harmonics approximation equation (SP_N) [13–15]. Each approximation model has its own advantages and disadvantages. For example, the DE is computationally effective but valid only in a high scattering medium; the higher order approximations, including S_N, P_N, PA, and SP_N, are accurate in media over a broad range of optical properties but computationally expensive compared with DE approximation [16]. These approximation models can effectively describe light propagation in a scattering medium; however, they are invalid in a nonscattering medium, except for S_N method, whose time cost is too expensive for practical applications.

A nonscattering medium, also called a void region, exists in some biological tissues, such as the stomach, esophagus, intestines, and bladder. Previous studies have shown that inaccurate reconstructed images would be obtained if the void region were not processed [17–20]. At present, several methods have been proposed to deal with light propagation in the

void region [21–29]. First, the RTE was adopted and coupled with the DE to describe light propagation in both high scattering and low scattering or nonscattering regions [21–23]. However, the computational complexity and expensive time cost of the RTE limits its extensive application to two-dimensional (2D) or 3D regular media [22,23]. Thus, it is not an ideal option for the inverse reconstruction of 3D optical imaging. Second, considering the golden accuracy of the Monte Carlo method, a hybrid Monte Carlo–diffusion method was proposed to deal with the low scattering or nonscattering problem, where the Monte Carlo method was employed to describe light propagation in the void region [24,25]. Although the Monte Carlo method provides excellent accuracy, it is time consuming due to the statistic characteristics and hardly ever applied to inverse reconstruction. The last approach is the hybrid radiosity–diffusion method (HRDM), in which the radiosity theory is used to describe light propagation in the void region [26–29]. Because of the high computational efficiency, the HRDM has been effectively applied to the inverse problem of optical imaging [17–20]. However, these studies mainly focused on a 2D or 3D regular medium. Furthermore, how much influence the void region would have on the accuracy of modeling light propagation has not been investigated, which is very important for 3D optical tomography.

In this paper, the HRDM was implemented with the FEM and verified with simulations in 3D complex models, including regular shape geometries and a digital mouse model. Results obtained from the simulation platform of the Molecular Optical Simulation Environment (MOSE) were utilized as the standard to verify the accuracy of the HRDM [30,31]. Furthermore, the influence of the void region on modeling light propagation in heterogeneous media were investigated. By changing the size of the void region, the results simulated by MOSE were compared with those calculated by the DE method. Taking the results of MOSE as the criterion, we tried to draw the conclusion that the influence of the void region can be neglected when its size is less than a certain range but must be taken into account in other cases. To avoid obtaining misleading results, we conducted a series of simulations with various geometries and optical properties. The rest of this paper is organized as follows. The mathematical formula of the HRDM and its numerical implementation are presented in the following section. In the third section, several simulation experiments are conducted to validate the accuracy of the HRDM and further discuss the influence of the void region on modeling light propagation in the heterogeneous medium. Finally, we provide a discussion and conclude this paper.

2. Mathematical Formula and Numerical Implementation

To deal with the void problem, an HRDM that couples the radiosity theory and the DE has been presented [26,28]. In this model, the radiosity theory integrated with the DE is utilized to describe the light transport in both the void and scattering regions. The HRDM-based light transport model is expressed as follows [32,33]:

$$-\nabla \cdot (D(r)\nabla \Phi(r)) + \mu_a(r)\Phi(r) = S(r),$$

$$\Phi(r) + 2A_n(r)D(r)(v(r) \cdot \nabla \Phi(r)) = 0,$$

$$S_0(r) = \int_B \frac{\Phi(r')}{2\pi A_n(r)} G(r,r')\mathrm{d}B',$$

$$G(r,r') = \xi(r,r') \frac{\cos \theta \cos \theta'}{|r-r'|^2} \exp(-\mu'_a|r-r'|), \quad (1)$$

where $\Phi(r)$ is the nodal photon flux density, $D(r)$ is the diffusion coefficient and is defined as $D(r) = (3(\mu_a(r) + \mu'_s(r)))^{-1}$, $\mu'_s(r)$ is the reduced scattering coefficient, $\mu_a(r)$ is the absorption coefficient, $S(r)$ is power density of the light source, and B is the boundary of void regions. A_n is the refractive mismatch factor at the boundary and is specified as $A_n = (1 + R(r))/(1 - R(r))$, where $R(r)$ can be calculated as $R(r) \approx -1.4399n^{-2} + 0.7099n^{-1} + 0.6681 + 0.0636n$ and n is the effective refractive index at the boundary [34,35]. $v(r)$ is the unit outer normal on the outer surface, $S_0(r)$ is a Neumann source formed at the interface of the scattering and void regions that has been included in the DE, and $G(r,r')$ is the transfer function between the points r' and r on the boundary B. $\xi(r,r')$ is the visibility factor and is defined as unity if r' and r are mutually visible; otherwise it is zero. θ and θ' are angles between the surface normal at r', r and unit directional vector $u(r,r') = (r-r')/|r-r'|$, and μ'_a is the absorption coefficient of the nonscattering region.

At the interface of the scattering and void regions, a Neumann source is formed by the light beam that transports across the void region, and it has been incorporated into the DE. The equivalent light source has the following formula:

$$S(r) = q(r) + S_0(r), \quad (2)$$

where $q(r)$ represents the internal light source.

Because of the excellent performance of the FEM in approaching complicated, irregular geometries, the FEM has been widely utilized in optical tomographic imaging [21–23,26,28,29,34]. Here, the FEM is also used to solve the HRDM-based light transport model. Thus, the Galerkin weighted residual method [29] is employed to expand the nodal photon flux density and the light source power density as the following expressions:

$$\Phi(r) = \sum_{i=1}^{N} \phi_i \varphi_i(r)$$

$$S(r) = \sum_{i=1}^{N} s_i \varphi_i(r), \quad (3)$$

where $\varphi_i(r)$ is the piecewise linear nodal basis function, ϕ_i and s_i represent the values at the ith node, and N is the total number of nodes in a finite element volume mesh. Substituting Eq. (3) into Eqs. (1) and (2), we obtain the following linear matrix equation that is composed of the FEM matrices:

$$M\Phi = FS, \qquad (4)$$

where $M = K + C + B - \Sigma$ and the related elements of the matrices are given as [29,35]

$$k_{ij} = \int_\Omega D(r)(\nabla \varphi_i(r)) \cdot (\nabla \varphi_j(r)) \mathrm{d}r,$$

$$c_{ij} = \int_\Omega \mu_a(r)\varphi_i(r)\varphi_j(r)\mathrm{d}r,$$

$$b_{ij} = \int_{\partial\Omega\cup\partial\Omega'} \frac{1}{2A_n(r)} \varphi_i(r)\varphi_j(r)\mathrm{d}r,$$

$$\Sigma_{ij} = \int_{\partial\Omega'} \int_{\partial\Omega'} \frac{1}{2\pi A_n(r')} G(r,r')\varphi_i(r)\varphi_j(r')\mathrm{d}S\mathrm{d}S',$$

$$f_{ij} = \int_\Omega \varphi_i(r)\varphi_j(r)\mathrm{d}r, \qquad (5)$$

where Ω is the solving domain constructed by the understudied geometry, $\partial\Omega$ is the outermost boundary of the domain, and $\partial\Omega'$ denotes the interface of the scattering and void regions.

3. Experiments and Results

In this section, two groups of experiments were conducted to verify the accuracy and effectiveness of the HRDM-based light transport model. First, the accuracy of the HRDM model was three-dimensionally validated, including using both the 3D regular geometries and the digital mouse geometry. Second, using the cyclic annular geometries, we systematically investigated how great an influence the void region's size would have on the modeling light propagation in a heterogeneous medium and discussed under what conditions the influence of the void region can be neglected.

A. Accuracy Verification Experiments

In this subsection, the accuracy of the HRDM model was validated using the regular shape geometries and a digital mouse model. Considering the high accuracy of the Monte Carlo method in simulating light propagation in a turbid medium, the software platform MOSE was selected as a standard to evaluate the results of the HRDM model [30,31].

To quantitatively evaluate the performance of the HRDM model, two evaluating factors were introduced, the average relative error (ARE) and the curve similarity (CS), and mathematically expressed by the following formulas [36]:

$$\mathrm{ARE} = \frac{\sum_{i=1}^N \left| \hat{f}_i^{\mathrm{MOSE}} - \hat{f}_i^{\mathrm{HRDM}} \right|}{N},$$

$$\mathrm{CS} = 1 - \frac{\sum_{i=1}^N (\hat{f}_i^{\mathrm{MOSE}} - \hat{f}_i^{\mathrm{HRDM}})^2}{\sum_{i=1}^N (\hat{f}_i^{\mathrm{MOSE}} - \overline{\hat{f}_i^{\mathrm{MOSE}}})^2}, \qquad (6)$$

where $\hat{f}_i$ is the normalized intensity and is defined as $\hat{f}_i = f_i/\max(f_i)$ $(i = 1, 2, ..., N)$ and N is the number of the sample point; the superscript MOSE represents that the intensity f was obtained by MOSE and HRDM for the HRDM model. $\overline{f_i^{\mathrm{MOSE}}}$ is the average intensity of all the sample points obtained by MOSE. ARE is the discrepancy between the calculated intensity of the HRDM model and the simulated one of MOSE, and CS is the correlation between them. Accordingly, the closer ARE gets to zero and the closer CS gets to unity, the better the performance of the HRDM model is.

1. 3D Regular-Geometry-Based Experiments
Three geometries were designed and employed to verify the accuracy of the HRDM model, including the sphere and cylinder geometries. Their geometrical parameters and the related optical properties are shown in Fig. 1 and Table 1, where Fig. 1(a) is the classical geometry employed in the existing studies [17–20,27,28] and Figs. 1(b) and 1(c) are
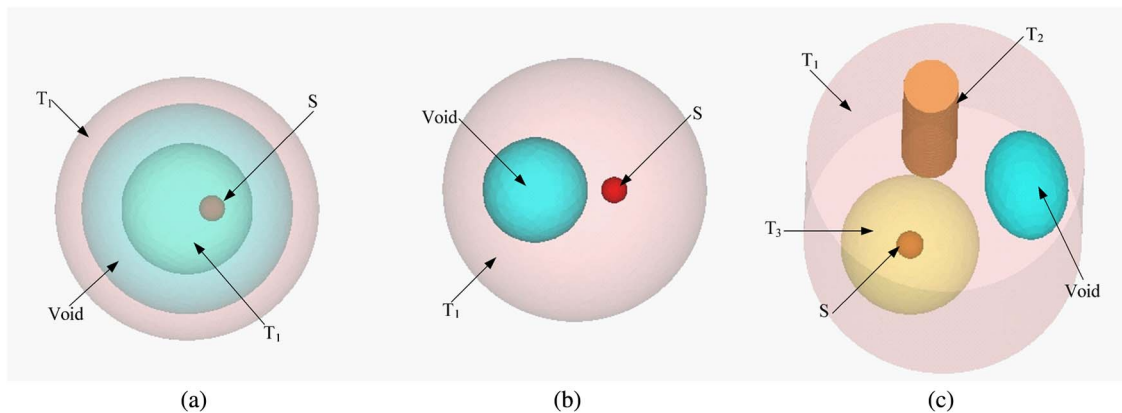

Fig. 1. (Color online) Experimental geometries employed in the comparisons: (a) is the comparison for the classical geometry in experiment No. 1; and (b) and (c) are those for the self-designed geometries used in experiments No. 2 and No. 3, respectively.

Table 1. Geometrical Parameters and the Related Optical Properties for the Three Different Regular Shape Geometries

Experiment No.	Tissue	Center	Radius	μ_a(mm^{-1})	μ_s'(mm^{-1})
1	T_1	(0, 0, 0)	(10, 10, 10)	0.05	1.2273
	Void	(0, 0, 0)	(4–7, 4–7, 4–7)	0.5	0.000001
	S	(2, 0, 0)	(1, 1, 1)	0.05	1.2273
2	T_1	(0, 0, 0)	(10, 10, 10)	0.05	1.2273
	Void	(3, 0, 0)	(4, 4, 4)	0.5	0.000001
	S	(−3, 0, 0)	(1, 1, 1)	0.05	1.2273
3	T_1	(0, 0, 0)	(10, 10, 10)	0.0049	1.2273
	Void	(−6, 0, 0)	(3, 4, 3)	0.05	0.0000001
	T_2	(0, −6, 0)	(2, 2, 8)	0.1021	2.4144
	T_3	(3, 3, 0)	(5, 5, 5)	0.2630	2.2091
	S	(3, 3, 0)	(1, 1, 1)	0.2630	2.2091

the geometries designed and utilized in this paper. To obtain an accurate and reliable simulated result of MOSE, a 100,000,000 photon simulation was performed to provide the comparison standards. To better illustrate the comparison, all of the results were normalized to the maximum value versus the detection positions. Figure 2 shows the comparison results for the detector at the z position: $z = 0$ mm, where Fig. 2(a) is the comparison for the classical geometry in experiment No. 1, and Figs. 2(b) and 2(c) are those for the self-designed geometries used in experiments No. 2 and No. 3, respectively. In Fig. 2, the solid red curves represent the simulated intensity of MOSE, and the blue asterisk curves show the calculated results of the HRDM model. Furthermore, the ARE and CS for the three geometries were calculated and listed in Table 2.

From Fig. 2 and Table 2, we find that similar tendencies and good agreement between the HRDM model and MOSE were obtained for the three different geometries, with the ARE less than 2% and the CS larger than 99%. Especially good agreement was obtained at the positions where the results were affected greatly by the void region, such as detection points 0–20 and 50–65 in Fig. 2(b) and points 20–35 in Fig. 2(c). In addition, the results, including both the simulated result of MOSE and the calculated result of the HRDM model, seem to be a little fluctuant, as shown in Fig. 2. This may be induced by

the stochastic nature of the Monte Carlo method and the mesh discretization of the HRDM model. The comparison results indicated that the HRDM model worked well in handling the void region problem and appeared in good agreement with the Monte Carlo method.

2. 3D Digital-Mouse-Based Experiment

In this subsection, a digital mouse was selected and used to verify the accuracy of the HRDM model in the case of complicated irregular shape geometry. The torso section of the digital mouse atlas was extracted from CT and cryosection data [37], and main organs were selected to simulate the tissue's heterogeneity, such as the muscle, heart, stomach, kidneys and lungs, as shown in Fig. 3. The detailed optical properties of each organ were calculated at a wavelength of about 650 nm and listed in Table 3 [38]. Therein, the stomach was artificially termed as the void region. To obtain the surface measurements, the torso of the digital mouse was discretized into 83,204 tetrahedral elements and 15,101 nodes.

To simulate the internal light source, a solid sphere of 1 mm radius was located around the center of the digital mouse with the coordinates (19, 9.6, 19) mm, which is beside the stomach. Similarly, the results obtained from the HRDM model and MOSE were all normalized to the maximum intensity versus the detection positions, and the comparison
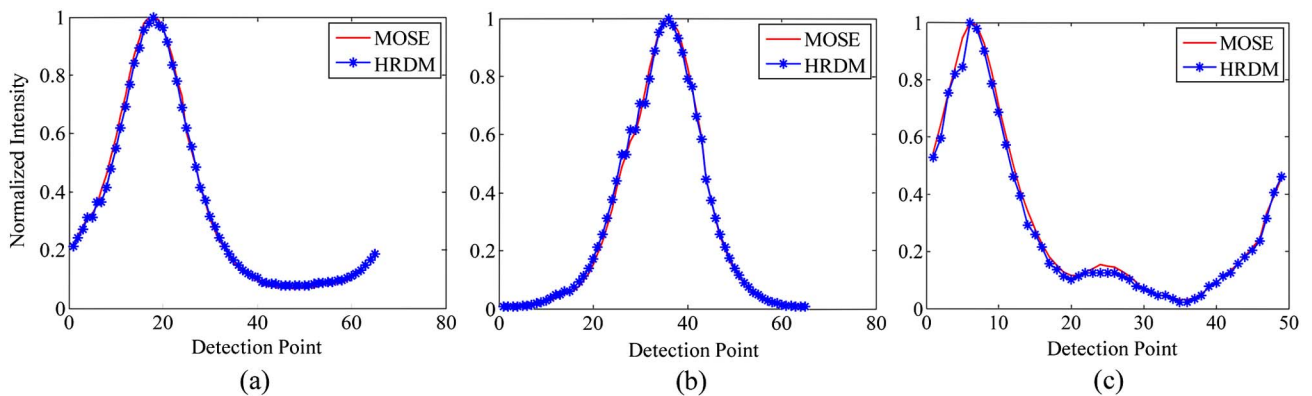

Fig. 2. (Color online) Comparisons of results between the calculated result of the HRDM model and the simulated one of MOSE. (a)–(c) Comparisons for the three kinds of geometries.

Table 2. Error Comparisons between the Calculated
Results of the HRDM Model and the Simulated
Ones of MOSE

Experiment No.	ARE	CS
1	0.0128	0.9969
2	0.0110	0.9976
3	0.0160	0.9936

Table 3. Optical Properties of the Main Organs of the Digital Mouse

Tissue	Muscle	Heart	Stomach	Kidney	Lung
μ_a	0.09428	0.07859	0.01504	0.08811	0.26296
μ_s'	2.29425	1.00656	0.0000001	2.35851	3.6818

results for the detector at three z positions ($z = 16.5$, 18.5, and 21.5 mm) were observed and presented in Fig. 4. Therein, the solid red curves denote the simulated results of MOSE, and the blue asterisk curves show the calculated results of the HRDM model. From Fig. 4, we find that similar tendencies were observed between the results of the HRDM model and those of MOSE. Although there is a slight difference at some detection points [in Figs. 4(a) and 4(c)], which was probably caused by the complicated and irregular structure of the digital mouse, good agreement was also obtained overall, with the ARE being about 0.0119 and the CS being about 0.9529. The preliminary results obviously demonstrated the high accuracy and effectiveness of the HRDM model in the complicated, irregular geometry.

B. Influence of the Size of the Void Region on Light Propagation

In this section, a group of comparison experiments were conducted to investigate the influence of the size of the void region on light propagation by artificially changing the size of the void region and then comparing the results of MOSE with those of the HRDM and DE models. Because of the high accuracy of the Monte Carlo method, the results simulated by MOSE were also selected as the standard to verify the accuracy of the DE model, in which the void problem was not considered. Simultaneously, to observe the effectiveness of the results calculated by the HRDM method, the results were also compared with MOSE. To better describe the size of the void region, the classical homocentric sphere geometry
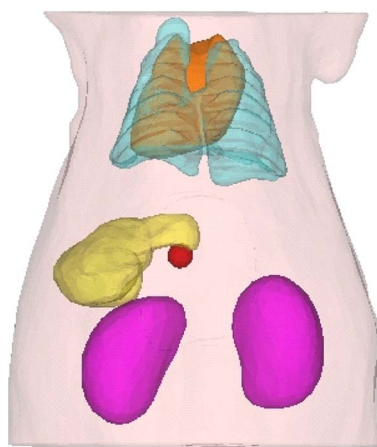

Fig. 3. (Color online) Digital mouse used in the complicated irregular-shape-geometry-based comparison experiment.

was utilized, which is similar to that used in Fig. 1(a). Similarly, the evaluation factors of ARE were also used to evaluate the comparison results, and it has the following new definition:

$$\text{ARE} = \frac{\sum_{i=1}^{N} |f_i - f_i^{\text{MOSE}}|}{N \max(f_i^{\text{MOSE}})}, \tag{7}$$

where the meanings of the parameters are similar to those in Eq. (6).

First, a similar geometry with identical optical properties to that used in Fig. 1(a) was employed to conduct the investigation. Here, the outer radius of the scattering T_1 was 17 mm. Based on the optical properties of the scattering region, the mean free path (MFP) of light propagation can be calculated as 0.7829 mm. To better characterize the changes of the void region's size, two parameters were defined: the inner radius and outer radius of the void region. By subtracting the inner radius from the outer radius, the size of the void region can be obtained. In the experiments, the inner radius was fixed to be 5 mm and the center of the light source was located at (3, 0, 0) mm. By changing the outer radius from 5.6 to 8.0 mm (5.6, 5.8, 6.0, 6.2, 6.4, 8.0 mm), different sizes of the void region can be obtained. In our evaluation, the size of the void region was characterized using a magnification of the absolute size. Figure 5 presents the comparison of the results among MOSE, HRDM, and DE at the central height of the geometry, where Figs. 5(a)–5(f) are the compared curves for the different sizes of the void region, which are scaled with the absolute size. In Fig. 5, the solid red curves represent the results of MOSE, and the blue asterisk curves and the green circle curves, respectively show those of the HRDM and DE models. Furthermore, as presented in Table 4, the quantitative comparison results were also calculated.

From Fig. 5 and Table 4, some interesting results are summarized. First, differences among the results of MOSE, HRDM, and DE were varied with the increasing size of the void region. The increase of the size of void region led to inaccuracy of the DE model, while the HRDM remained perfect. Second, when the size of void region was below the value of 0.8 mm, which is about 1 MFP, the DE model performed as perfectly as the HRDM. The performance of the DE model can also be accepted when the size of the void region is in the range 0.8 to 1.2 mm (about 1.5 MFPs). In the other cases, the DE model broke down. As a result, we conclude that the influence of the void region on the light propagation can be neglected when the size of the void region is located below a certain range such as 1.2 mm (about 1.5
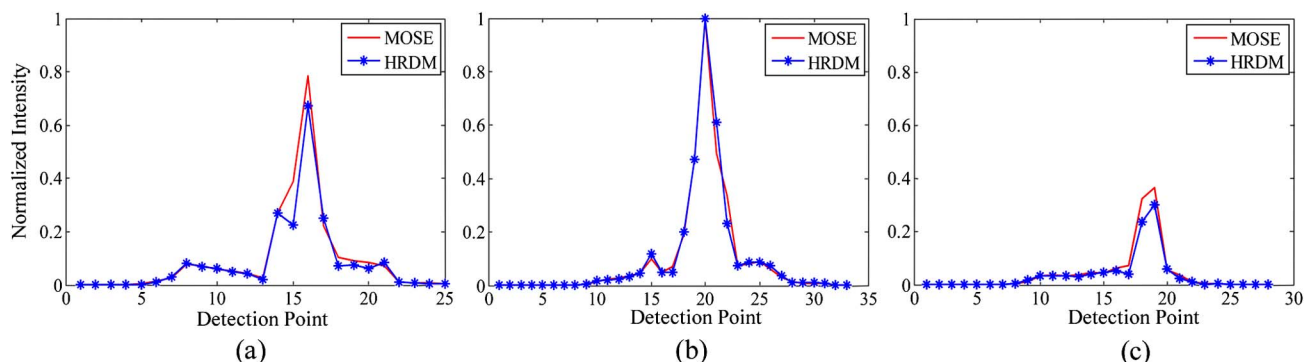
Fig. 4. (Color online) Comparisons of the digital-mouse-based experiment between the calculated results of the HRDM model and the simulated ones of MOSE. (a)–(c) Compared curves at a height of $z = 16.5$, 18.5, and 21.5 mm, respectively.
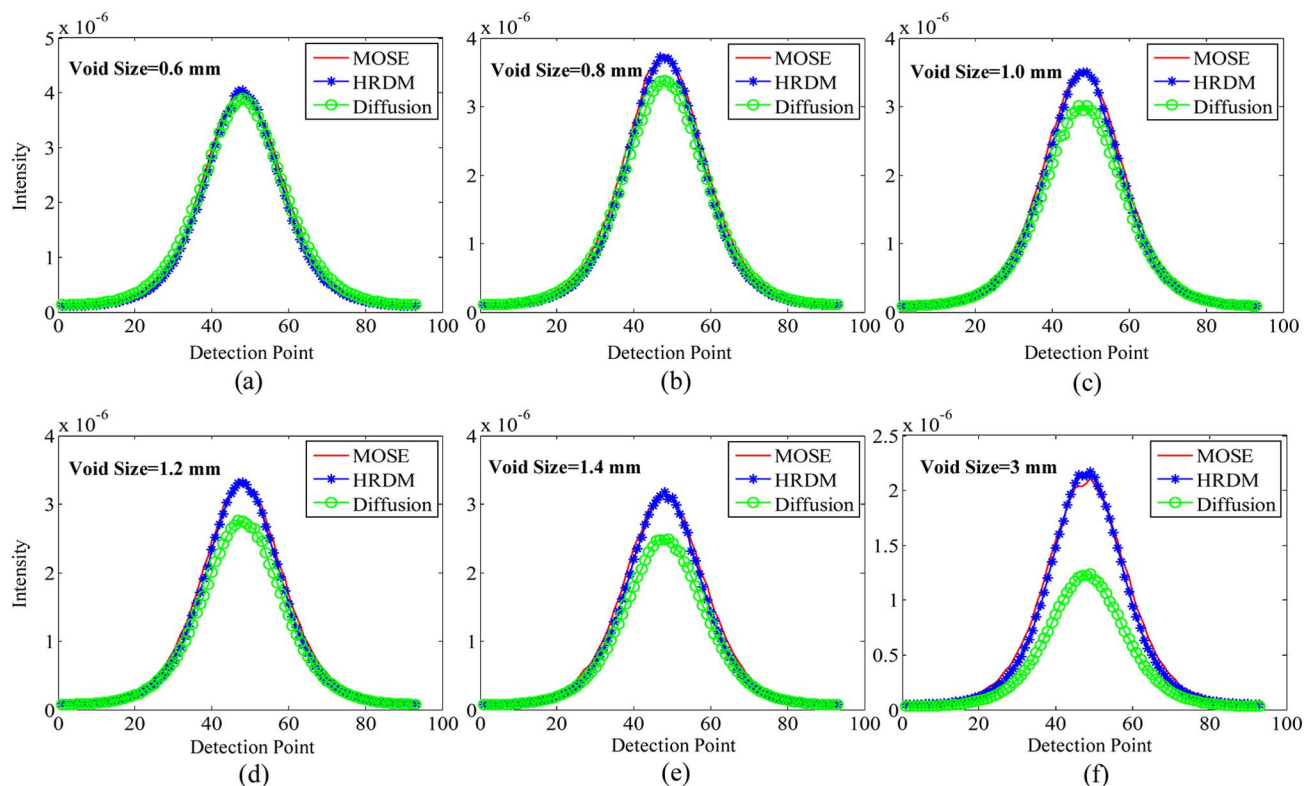

Fig. 5. (Color online) Compared results among the MOSE simulation, the HRDM calculated, and the DE calculated when the size of the void region was varied. (a)–(f) Comparison results of different sizes of the void region.

MFPs) in this experiment. In other words, the void problem must be taken into account if the size of the void region is too large such as 3 mm in this experiment, which is an important conclusion for 3D

Table 4. Compared Results of the ARE Values of MOSE versus the DE and of MOSE versus the HRDM

Experiment No.	Void Size (mm)	MOSE versus DE	MOSE versus HRDM
a	0.6	0.0083	0.0223
b	0.8	0.0302	0.0236
c	1.0	0.0470	0.0237
d	1.2	0.0555	0.0220
e	1.4	0.0668	0.0245
f	3.0	0.1313	0.0230

optical imaging, including both the forward and inverse problems. In order to eliminate the influence of other factors on our conclusion, such as the size and optical properties of the scattering region, two other experiments were also performed in the following sections.

1. Investigation of the Size of Scattering Region as an Accidental Factor

In order to eliminate the size of the scattering region as an accidental factor, two additional experiments were performed. We changed the size of the geometry but kept the same optical properties as those used in Fig. 1(a). In the two additional experiments, the MFPs were all the same as in the original experiment. By changing the outer radius of the scattering

region T_1 to 13 or 10 mm, three groups of experiments were obtained. In this section, the experiment with the outer radius of the scattering region as 17 mm was defined as the original experiment, and those of 13 and 10 mm were defined as the first additional and the second additional experiment, respectively. For the two additional groups of experiments, the center of the light source for the first additional experiment was located at (3, 0, 0) mm with a radius of 1 mm, while the second additional one was located at (2, 0, 0) mm. Accordingly, to obtain the different sizes of the void region, the outer radius of the void region for the first additional group of experiments was changed from 5.6 to 7.0 mm (5.6, 5.8, 6.0, 6.2, 6.4, 6.6, 6.8, 7.0 mm), while for the second additional group of experiments it was changed from 4.6 to 6.0 mm (4.6, 4.8, 5.0, 5.2, 5.4, 5.6, 5.8, 6.0 mm). Similarly, the size of the void region was also characterized using the magnification of the absolute size. Figure 6 shows the variation of ARE versus the absolute size. In Fig. 6, the red diamond curves, the cyan triangle curves, and the black square curves represent the comparison results between MOSE and the DE for the original, the first additional, and the second additional experiment, respectively. Similarly, the magenta asterisk dotted curves, the blue cross dotted curves, and the orange circle dotted curves show the comparison results between MOSE and the HRDM for the original, the first additional, and the second additional experiment, respectively. The green dashed line is the standard line under which the influence of the void can be neglected. The value of the standard line was set to be 0.05 as the threshold value for ARE.

The evaluation factor ARE versus the absolute size of the void region is similar for all three experiments. For the three experiments, the DE worked as perfectly as the HRDM when the size of the void region was below the value of 0.8 mm (about one MFP), and the performance of the DE model can be accepted when the size of the void region reached 1.2 mm (about 1.5 MFPs). The performance of the HRDM
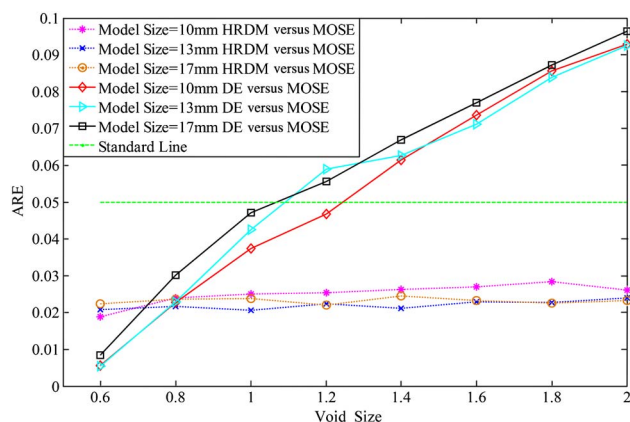

Fig. 6. (Color online) Variation of evaluation factor ARE versus the absolute void sizes corresponding to the different sizes of the scattering region.

method remained at an almost perfect level. Therefore, we can conclude that the influence of the size of void region on the accuracy of light propagation was uncorrelated with the size of the scattering region, which eliminated the scattering region's size as an accidental factor in the conclusion addressed above.

2. Investigation of the Optical Properties of the Scattering Region as an Accidental Factor

In this subsection, the aim was to investigate the influence of the optical properties of the scattering region. The original group of experiments was the same as the second additional one in the above section. Therefore, another four additional experiments were performed to investigate the influence of the optical properties, including the absorption coefficient and the scattering coefficient, on our conclusion. In the four additional experiments, the same geometry as that used in Fig. 1(a) but with different optical properties was employed to conduct the investigation. The size of the void region was also characterized using the magnification of the absolute size. The first two additional experiments were performed to observe the absorption coefficient as an accidental factor, while the other two additional experiments were performed to investigate the scattering coefficient as an accidental factor.

In the first two additional experiments, we changed the absorption coefficient from 0.025 to 0.8 mm^{-1} (0.025, 0.08 mm^{-1}) while keeping the scattering coefficient of 12.273 mm^{-1}, and they were defined as the first additional experiment and the second additional experiment, respectively. For the first and second additional experiments, the sizes of the void regions were all changed from 4.6 to 6.0 mm (4.6, 4.8, 5.0, 5.2, 5.4, 5.6, 5.8, 6.0 mm), and the MFPs were, respectively 0.7986 and 0.4933 mm. In the other two additional experiments, the scattering coefficient was changed from 15.5 to 19.5 mm^{-1} (15.5, 19.5 mm^{-1}) while the absorption coefficient was kept as 0.05 mm^{-1}, and these were defined as the third additional experiment and the fourth additional experiment. The MFPs corresponding to the third and the fourth additional experiments were, respectively 0.625 and 0.5 mm. For the third and the fourth additional experiments, variations of the size of the void region corresponded to the following lists: (4.5, 4.8, 5.0, 5.2, 5.5, 5.8, 6, 6.5 mm) and (4.5, 4.8, 5.0, 5.2, 5.5, 5.8, 6, 6.5 mm).

Figure 7 presents the variation of the evaluation factor versus the absolute size of the void region. Figure 7(a) presents the variation of evaluation factor ARE for the first two additional experiments and the original one, while Fig. 7(b) gives those for the second two additional experiments and the original one. In Fig. 7, the red diamond curves represent the comparison results between MOSE and the DE for the original experiment, the cyan triangle curves represent the comparison results between MOSE and the DE for the first additional experiment in
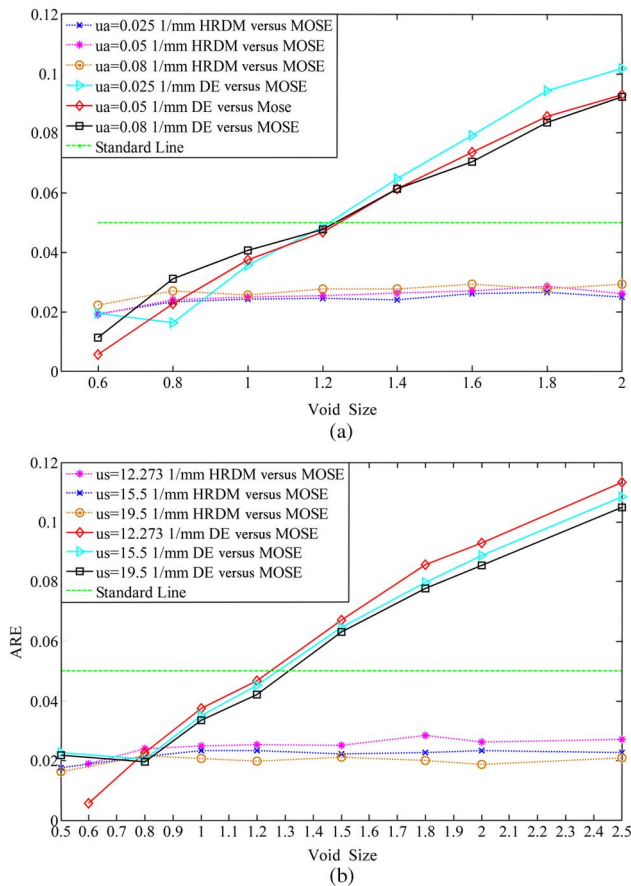
Fig. 7. (Color online) Variation of evaluation factors versus the absolute size of the void region. (a) Variation of ARE versus the void sizes corresponding to the original, the first, and the second additional experiment, which have different absorption coefficients, and (b) variation of ARE versus the absolute sizes of the void regions corresponding to the original, the third, and the fourth additional experiment, which have different scattering coefficients.

Fig. 7(a) and the third additional one in Fig. 7(b), and the black square curves show the results between MOSE and the DE for the second additional experiment in Fig. 7(a) and the fourth additional one in Fig. 7(b). The magenta asterisk dotted curves, the blue cross dotted curves, and the orange circle dotted curves show the comparison results between MOSE and the HRDM for the original experiment in both Figs. 7(a) and 7(b), of the first additional experiment in Fig. 7(a) and the third one in Fig. 7(b), and of the second additional experiment in Fig. 7(a) and the fourth one in Fig. 7(b), respectively. Similarly, the green dashed line is also the standard line.

In Fig. 7, the same conclusion can also be addressed: that the influence of the void region on the light propagation must be taken into account when the size of the void region is larger than a certain value, such as 1.2 mm (about 1.5 MFPs in the original experiment, about 1.5 MFPs in the first additional one, about 2.4 MFPs in the second one, about 2 MFPs in the third additional one, and about 2.4 MFPs in the fourth one). The phenomenon that the ARE between MOSE and the DE increased

linearly with the increase of the size of the void region can also be demonstrated in this subsection.

4. Conclusion and Discussion

A void region exists in some biological tissues, and previous studies have shown that inaccurate images would be obtained if it was not processed in a modeling light transport [18]. In previous studies, an HRDM-based light transport model has been proposed, in which the radiosity theory was coupled into the DE to handle the void problem, and it has been well demonstrated in 2D and 3D simple homocentric sphere models. In this paper, we have validated the accuracy of the HRDM-based model in different 3D models, including both the regular geometries and a digital mouse model. Importantly, the influence of the void region on modeling the light propagation in a heterogeneous medium was also quantitatively investigated in this paper for the first time, to the best of our knowledge. Useful conclusions were also obtained from our experiments. First, the influence of the void region can be neglected when the size of the void region is below a certain range, which is commonly regarded as below 2 MFPs, and must be taken into account when the size of the void region is too large. Second, the influence of the void on light propagation is nearly a linear relation with the size of the void region. The knowledge of the influence of the void region on the accuracy of the light propagation is significantly important in the study of optical imaging. Having a good knowledge of this *a priori* information, we can establish an appropriate light transport model with a compromise between accuracy and efficiency. Our investigation results not only provide experimental support for the previous study [17–20] but also present a quantitative knowledge of the influence of the void region on the accuracy of the light propagation.

However, there is an inevitable shortcoming for the HRDM-based model. Because of the limitations of the DE, the HRDM-based model worked in the coupled high scattering and void region, but it was invalid in the coupled low scattering and void region. Actually, the low scattering regions commonly exist in the animal body and must be considered for whole-body small animal optical imaging. As a result, our future work will focus on the development of a hybrid light transport model that can be used to depict the light propagation in any scattering region. The corresponding results will be reported later.

References

1. S. R. Arridge and J. C. Hebden, "Optical imaging in medicine. 2. modelling and reconstruction," Phys. Med. Biol. **42**, 841–853 (1997).
2. A. P. Gibson, J. C. Hebden, and S. R. Arridge, "Recent advances in diffuse optical imaging," Phys. Med. Biol. **50**, R1–R43 (2005).
3. J. Tian, J. Bai, X. Yan, S. Bao, Y. Li, W. Liang, and X. Yang, "Multimodality molecular imaging," IEEE Eng. Med. Biol. Mag. **27**, 48–57 (2008).
4. R. Weissleder and V. Ntziachristos, "Shedding light onto live molecular targets," Nat. Med. **9**, 123–128 (2003).
5. V. Ntziachristos, J. Ripoll, L. H. V. Wang, and R. Weissleder, "Looking and listening to light: the evolution of whole-body photonic imaging," Nat. Biotechnol. **23**, 313–320 (2005).
6. A. Ishimaru, *Wave Propagation and Scattering in Random Media* (Academic, 1978).
7. A. D. Klose, V. Ntziachristos, and A. H. Hielscher, "The inverse source problem based on the radiative transfer equation in optical molecular imaging," J. Comput. Phys. **202**, 323–345 (2005).
8. L. V. Wang and H.-I. Wu, *Biomedical Optics: Principle and Imaging* (Wiley, 2007).
9. K. Peng, X. Gao, X. Qu, N. Ren, X. Chen, X. He, X. Wang, J. Liang, and J. Tian, "Graphics processing unit parallel accelerated solution of the discrete ordinates for photon transport in biological tissues," Appl. Opt. **50**, 3808–3823 (2011).
10. Z. Yuan, X.-H. Hu, and H. Jiang, "A higher order diffusion model for three-dimensional photon migration and image reconstruction in optical tomography," Phys. Med. Biol. **54**, 65–88 (2009).
11. S. Wright, M. Schweiger, and S. R. Arridge, "Reconstruction in optical tomography using the PN approximations," Meas. Sci. Technol. **18**, 79–86 (2007).
12. W. Cong, A. Cong, H. Shen, Y. Liu, and G. Wang, "Flux vector formulation for photon propagation in the biological tissue," Opt. Lett. **32**, 2837–2839 (2007).
13. A. D. Klose and E. W. Larsen, "Light transport in biological tissue based on the simplified spherical harmonics equations," J. Comput. Phys. **220**, 441–470 (2006).
14. Y. Lu, A. Douraghy, H. B. Machado, D. Stout, J. Tian, H. Herschman, and A. F. Chatziioannou, "Spectrally resolved bioluminescence tomography with the third-order simplified spherical harmonics approximation," Phys. Med. Biol. **54**, 6477–6493 (2009).
15. K. Liu, Y. Lu, J. Tian, C. Qin, X. Yang, S. Zhu, X. Yang, Q. Gao, and D. Han, "Evaluation of the simplified spherical harmonics approximation in bioluminescence tomography through heterogeneous mouse models," Opt. Express **18**, 20988–21002 (2010).
16. A. D. Klose, "The forward and inverse problem in tissue optics based on the radiative transfer equation: a brief review," J. Quant. Spectrosc. Radiat. Transfer **111**, 1852–1853 (2010).
17. H. Dehghani, D. T. Delpy, and S. R. Arridge, "Photon migration in non-scattering tissue and the effects on image reconstruction," Phys. Med. Biol. **44**, 2897–2906 (1999).
18. H. Dehghani, S. R. Arridge, M. Schweiger, and D. T. Delpy, "Optical tomography in the presence of void regions," J. Opt. Soc. Am. A. **17**, 1659–1670 (2000).
19. J. Riley, H. Dehghani, M. Schweiger, S. R. Arridge, J. Ripoll, and M. Nieto-Vesperinas, "3D optical tomography in the presence of void regions," Opt. Express **7**, 462–467 (2000).
20. H. Dehghani and D. T. Delpy, "Linear single-step image reconstruction in the presence of nonscattering regions," J. Opt. Soc. Am. A. **19**, 1162–1171 (2002).
21. T. Tarvainen, M. Vauhkonen, V. Kolehmainen, S. R. Arridge, and J. P. Kaipio, "Coupled radiative transfer equation and diffusion approximation model for photon migration in turbid medium with low-scattering and non-scattering regions," Phys. Med. Biol. **50**, 4913–4930 (2005).
22. T. Tarvainen, M. Vauhkonen, V. Kolehmainen, and J. P. Kaipio, "Finite element model for the coupled radiative transfer equation and diffusion approximation," Int. J. Numer. Meth. Eng. **65**, 383–405 (2006).
23. D. Gorpas, D. Yova, and K. Politopoulos, "A three-dimensional finite elements approach for the coupled radiative transfer equation and diffusion approximation modeling in fluorescence imaging," J. Quant. Spectrosc. Radiat. Transfer **111**, 553–568 (2010).
24. T. Hayashi, Y. Kashio, and E. Okada, "Hybrid Monte Carlo–diffusion method for light propagation in tissue with a low-scattering region," Appl. Opt. **42**, 2888–2896 (2003).
25. Y. Ogoshi and E. Okada, "Analysis of light propagation in a realistic head model by a hybrid method for optical brain function measurement," Opt. Rev. **12**, 264–269 (2005).
26. M. Firbank, S. R. Arridge, M. Schweiger, and D. T. Delpy, "An investigation of light transport through scattering bodies with non-scattering regions," Phys. Med. Biol. **41**, 767–783 (1996).
27. J. Ripoll, M. Nieto-Vesperinas, S. R. Arridge, and H. Dehghani, "Boundary conditions for light propagation in diffusive media with nonscattering regions," J. Opt. Soc. Am. A. **17**, 1671–1681 (2000).
28. S. R. Arridge, H. Dehghani, M. Schweiger, and E. Okada, "The finite element model for the propagation of light in scattering media: a direct method for domains with nonscattering regions," Med. Phys. **27**, 252–264 (2000).
29. J. H. Lee, S. Kim, and Y. T. Kim, "Modeling of diffuse-diffuse photon coupling via a nonscattering region: a comparative study," Appl. Opt. **43**, 3640–3655 (2004).
30. H. Li, J. Tian, F. P. Zhu, W. X. Cong, L. V. Wang, E. A. Hoffman, and G. Wang, "A mouse optical simulation environment (MOSE) to investigate bioluminescent phenomena in the living mouse with the Monte Carlo method," Acad. Radiol. **11**, 1029–1038 (2004).
31. N. Ren, J. Liang, X. Qu, J. Li, B. Lu, and J. Tian, "GPU-based Monte Carlo simulation for light propagation in complex heterogeneous tissues," Opt. Express **18**, 6811–6823 (2010).
32. X. Chen, J. Liang, J. Liu, H. Hu, X. Qu, F. Wang, and Y. Nie, "Multi-modality molecular imaging for gastric cancer detection," Proc. SPIE **8311**, 831115 (2011).
33. X. Chen, D. Yang, X. Qu, H. Hu, J. Liang, X. Gao, and J. Tian, "Comparisons of hybrid radiosity-diffusion model and diffusion equation for bioluminescence tomography in cavity cancer detection," J. Biomed. Opt. **17**, 066015 (2012).
34. M. Schweiger, S. R. Arridge, M. Hiraoka, and D. T. Delpy, "The finite element method for the propagation of light in scattering media: boundary and source conditions," Med. Phys. **22**, 1779–1792 (1995).
35. W. X. Cong, G. Wang, D. Kumar, Y. Liu, M. Jiang, L. V. Wang, E. A. Hoffman, G. McLennan, P. B. McCray, J. Zabner, and A. Cong, "Practical reconstruction method for bioluminescence tomography," Opt. Express **13**, 6756–6771 (2005).
36. X. Chen, X. Gao, X. Qu, D. Chen, X. Ma, J. Liang, and J. Tian, "Generalized free-space diffuse photon transport model based on the influence analysis of a camera lens diaphragm," Appl. Opt. **49**, 5654–5664 (2010).
37. B. Dogdas, D. Stout, A. F. Chatziioannou, and R. M. Leahy, "Digimouse: a 3D whole body mouse atlas from CT and cryosection data," Phys. Med. Biol. **52**, 577–587 (2007).
38. G. Alexandrakis, F. R. Rannou, and A. F. Chatziioannou, "Tomographic bioluminescence imaging by use of a combined optical-PET (OPET) system: a computer simulation feasibility study," Phys. Med. Biol. **50**, 4225–4241 (2005).